A Finite Piece Method for Simulating Polymer Melt Flows in Extrusion Sheet Dies

Yong Li, Jianrong Zheng, Chunmin Xia, Wei Zhou

Department of Mechanical Engineering, School of Mechanical and Power Engineering, East China University of Science and Technology Shanghai, 200237, People's Republic of China

Received 26 October 2010; accepted 26 May 2011
DOI 10.1002/app.34979
Published online 2 September 2011 in Wiley Online Library (wileyonlinelibrary.com).

ABSTRACT: A finite piece method is proposed to simulate three-dimensional slit flows in extrusion sheet dies in this paper. The simulations concern incompressible fluids obeying different constitutive equations: generalized Newtonian (Carreau-Yasuda law), and viscoelastic Phan-Thien Tanner (PTT) models. Numerical simulations are carried out for the isothermal and nonisothermal flows of polymer melt through sheet dies. The Picard iteration method is utilized to solve nonlinear equations. The results of the finite piece method are compared with the three-dimensional (3D) finite element method (FEM) simulation and experiments. At the die exit, the relative error of the volumetric flow between the finite piece method and the 3D FEM is below 1.2%. The discrepancy of the pressure distributions does not exceed 6%. The Maximum error of the uniformity index between the simulations and experiments is about 2.3%. It shows that the solution accuracy of the finite piece method is excellent, and a substantial amount of computing time and memory requirement can be saved. © 2011 Wiley Periodicals, Inc. J Appl Polym Sci 123: 3189–3198, 2012

Key words: polymer extrusion; viscoelastic properties; simulations; PTT constitutive equation; the finite element method

INTRODUCTION

The manufacture of plastic films and sheets is frequently accomplished by using the so-called fish-tail or coat-hanger dies, in which the polymeric fluid flows through the gap with large ratio of width to thickness. The slit flow is a typical problem for this kind of dies. The main rheological concern in the design of the channels is to obtain as uniform a melt flow distribution as possible. Obviously, knowledge of how a shear thinning and viscoelastic polymer melts flow inside the various die sections is necessary for proper design.

Traditional FEM can handle the 3D flow problem of the polymer melt. In some of the numerical studies, the flows of the polymer melt in sheet dies have been simulated using the 3D FEM to solve for the pressures, velocities, and temperatures.[1–5] Various generalized Newtonian fluid models have been included in these simulations. But an exact mathematical analysis of viscoelastic flows in the dies is a very challenging proposition because of the complexities with geometrical and viscoelastic effects.

On the other hand, it can be justified that the polymeric fluid motion follows the two-dimensional (2D) Hele Shaw model[6] between the gaps in the sheet dies. The 2D simulations provide a computationally efficient alternative to the 3D methods. Vlcek et al.[7] used a control volume method to performed a 2D simulation on the flow distribution in slit dies. Liu et al.[8] combined both the simple one-dimensional lubrication approximation and the 3D finite element simulation to design the extrusion sheet die for viscoplastic fluids with a Bingham model. Yu[9] divided the flow regime into 2D and 3D regions, and proposed a hybrid 3D/2D FEM to simulate motions of Carreau fluid. Moreover, nonisothermal flows in coat-hanger dies have been investigated in some studies.[10] Arpin et al.[11] developed a new model using a modified flow analysis network method for the calculation of the 2D flow inside a coat-hanger die, coupled with a finite-difference scheme for the calculation of temperature. The die body was also analyzed coupled to the melt flow analysis to minimize the die-inlet pressure.[12,13] Smith et al.[14,15] performed optimization of extrusion sheet dies by using a gradient-based optimization algorithm to minimize the total pressure drop across the die and reduce the velocity variation at the die exit.

Among the constitutive models used in the polymer flow simulation, the nonlinear PTT[16] constitutive equation provides a better fitting to the rheology of polymer melts than other simpler models such as power-law, the upper convected Maxwell or Oldroyd-B. And it is usually used to test the efficiency of numerical method. The numerical study using

Correspondence to: Y. Li (yong_li@ecust.edu.cn).

this model was initiated with the simulation of 2D and 3D steady contraction flow.[17–21] More recent studies consider 3D extrusion flows[22] and 3D free surface flows.[23] But it is only used in some simple flow channels of the 3D problems.

The channel of the sheet dies is wide and thin gaps, and the primary focus of most sheet die designs is the development of a uniform velocity across the width of the die exit. In addition geometrical complexity and rheological behavior lead to a huge CPU and pro-process time required for 3D simulations of viscoelastic flows in the dies. Therefore a complete 3D analysis is unnecessary. In this study, a finite piece method is established to predict the isothermal and nonisothermal viscoelastic flow through a planar slit channel. It is a finite element semianalytical method which can be adopted to reduce the computation memory requirement for 3D problems. The mathematical model of the 3D flows through the sheet dies is established with Carreau-Yasuda and PTT constitutive model. The SU technology[24] is employed to improve the computation stability. The flows of LLDPE polymer melts in two kinds of sheet dies are analyzed and the results are compared with those from 3D FEM and Arpin's experiments.[11]

Governing equations

The flow is governed by the general equations for mass and momentum. Considering the characteristics of the polymer melts flow in a die channel, for an incompressible fluid under creeping flow conditions ($R_e = 0$), the motion equation and the continuity equation are given by:

$$-\nabla P + \nabla \cdot \tau = 0 \tag{1}$$

$$\nabla \cdot \mathbf{V} = 0 \tag{2}$$

where P is the isotropic pressure, τ is the extrastress tensor, V is the velocity vector.

Rheological models of two types are adopted for the simulations. For a non-Newtonian (generalized Newtonian) fluid, τ is expressed by the equation:

$$\tau = 2\eta(\mathrm{II}_D)\mathbf{D} = 2\eta(\mathrm{II}_D)(\nabla\mathbf{V} + \nabla\mathbf{V}^T) \tag{3}$$

where $\mathbf{D}$ is the rate of strain tensor, the non-Newtonian viscosity obeys a Carreau-Yasuada law such that:

$$\eta(\mathrm{II}_D) = \eta_0(1 + (\lambda\dot{\gamma})^a)^{(n-1)/a} \tag{4}$$

where $\dot{\gamma} = (2\Pi_D)^{1/2}$ and Π_D is the second invariant of the rate of strain tensor. a, n, and λ are constants.

For a viscoelastic fluid, the polymer extrastress tensor can be splited into a purely viscous part and a polymeric contribution:

$$\tau = \tau_s + \mathbf{S} \tag{5}$$

here $\mathbf{S}$ is the extrastress tensor due to viscoelasticity and τ_s is the stress component of pure Newtonian fluid given by

$$\tau_s = 2\eta_s\mathbf{D} \tag{6}$$

where η_s is the Newtonian-contribution solvent viscosity. To complete the description, a constitutive equation that describes the rheology of the fluid is required to determine the polymeric part of the extra stress tensor. The constitutive equation for a PTT fluid may be expressed as:

$$Y(\mathbf{S})\mathbf{S} + \lambda[(1 - \xi/2)\overset{\nabla}{\mathbf{S}} + (\xi/2)\overset{\Delta}{\mathbf{S}}] = 2\eta_v\mathbf{D} \tag{7}$$

In the above equations, $\overset{\nabla}{\mathbf{S}}$ and $\overset{\Delta}{\mathbf{S}}$ denote, respectively, the contravariant and the covariant derivatives of the stress tensor:

$$\overset{\nabla}{\mathbf{S}} = (\mathbf{V} \cdot \nabla)\mathbf{S} - \nabla\mathbf{V}^T \cdot \mathbf{S} - \mathbf{S} \cdot \nabla\mathbf{V} \tag{8}$$

$$\overset{\Delta}{\mathbf{S}} = (\mathbf{V} \cdot \nabla)\mathbf{S} + \mathbf{S} \cdot (\nabla\mathbf{V})^T + \nabla\mathbf{V} \cdot \mathbf{S} \tag{9}$$

The stress function $Y(S)$ follows the exponential form:

$$Y(\mathbf{S}) = \exp((\varepsilon\lambda/\eta_v)Tr\mathbf{S} \tag{10}$$

In the above equations, λ is the relaxation time, η_v is the zero shear polymer viscosity. The total viscosity $\eta_0 = \eta_s + \eta_v$. PTT models have two scalar parameters which can be used to control viscoelastic. The parameter ξ governs the ratio of the first to the second normal stress. The other parameter ε imposes an upper limit to the elongational viscosity, which increases as this parameter decreases.

For the nonisothermal flow, the energy equation is express as:

$$\rho C_p \frac{DT}{Dt} = k\nabla^2 T + \tau : \mathbf{D} \tag{11}$$

where T is the temperature, ρ denotes the fluid density, k is the thermal conductivity, C_p is the heat capacity. The temperature dependence of the viscosity and the relaxation time is described by using a shift factor $A(T)$ and $B(T)$. Accordingly, the viscosity η_0 and the relaxation time λ are expressed in terms of the temperature by means of the following relations:

$$\eta_0(T) = A(T)\eta_0(T_0) \tag{12}$$

$$\lambda(T) = B(T)\lambda(T_0) \tag{13}$$

In these equations, η_0 (T_0) and λ (T_0) denote the respective viscosity and relaxation time at a reference temperature T_0. The shift factor are given by[11]

$$A(T) = \exp\left(C_1\left(\frac{1}{T} - \frac{1}{T_0}\right)\right) \tag{14}$$

$$B(T) = \exp\left(C_2\left(\frac{1}{T} - \frac{1}{T_0}\right)\right) \tag{15}$$

where C_1 and C_2 are the WLF parameters.

For the slit flow channel, the size of thickness is much less than others. We postulate the pressure does not change along the thickness direction and create Cartesian coordinate system which the Z axis is along the thickness direction of the slit channel, as shown in Figure 1, so the eqs. (1) and (2) can be rewritten as the component type:

$$-\frac{\partial p}{\partial x} + \frac{\partial \tau_{xx}}{\partial x} + \frac{\partial \tau_{yx}}{\partial y} + \frac{\partial \tau_{zx}}{\partial z} = 0 \tag{16}$$

$$-\frac{\partial p}{\partial y} + \frac{\partial \tau_{xy}}{\partial x} + \frac{\partial \tau_{yy}}{\partial y} + \frac{\partial \tau_{xz}}{\partial z} = 0 \tag{17}$$

$$-\frac{\partial p}{\partial z} = 0 \tag{18}$$

$$\frac{\partial v_x}{\partial x} + \frac{\partial v_y}{\partial y} + \frac{\partial v_z}{\partial z} = 0 \tag{19}$$

Postulating the lower surface of the channel is h_1 (x,y), the upper surfaces is h_2 (x,y), the integral of eq. (19) along the thickness is

$$\int_{h_1}^{h_2} \frac{\partial v_x}{\partial x} dz + \int_{h_1}^{h_2} \frac{\partial v_y}{\partial y} dz + \int_{h_1}^{h_2} \frac{\partial v_z}{\partial z} dz = 0 \tag{20}$$

and defining the volumetric flow as follow:

$$q_x = \int_{h_1}^{h_2} v_x dz \tag{21}$$

$$q_y = \int_{h_1}^{h_2} v_y dz \tag{22}$$

we obtain:

$$\frac{\partial q_x}{\partial x} + \frac{\partial q_y}{\partial y} = v_x(h_2)\frac{\partial h_2}{\partial x} + v_y(h_2)\frac{\partial h_2}{\partial y} - v_z(h_2) - \left[v_x(h_1)\frac{\partial h_1}{\partial x} + v_y(h_1)\frac{\partial h_1}{\partial y} - v_z(h_1)\right] \tag{23}$$

It can be found that the right end item is the normal velocity of the upper and lower surface which is obviously zero, so the continuity equation related to the volumetric flow is:

$$\frac{\partial q_x}{\partial x} + \frac{\partial q_y}{\partial y} = 0 \tag{24}$$

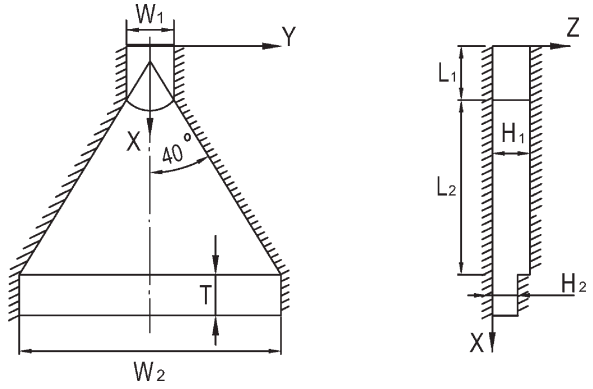

Figure 1 Schematic diagram of the fish-tail die channel and the coordinate system.

Numerical scheme

The length and width of sheet dies in the X, Y direction is much longer than the thickness in the Z direction, and a well-designed die shall provide smooth and uniform flow in the X-Y plane. Thus the key issue of the simulation is to acquire the flow distribution in the X, Y direction. Since the flow without secondary flow (e.g., vortex) is creeping, the flow channel with varying thickness can be divided into several small parallel regions (elements) of different height. The flow inside the element can be assumed to be the same as those inside the parallel flow channel; also the velocity v_z and extrastress S_{zz} can be ignored. Because the velocity and extrastress are still the function of the coordinate Z, it still remains to be a 3D problem. The finite piece method which is one of the finite element semianalysis methods with volumetric flow as unknown variables will be utilized to calculate the flow distribution of the X, Y plane. In this way, the key issue mentioned above can be simplified to a 2D solving procedure to obtain final solution.

For the finite piece method, the distribution functions of the velocity v_x, v_y and the extrastress $\mathbf{S}$ tensor related to the Z direction is assumed to be known so that the finite element interpolating polynomial can be constructed without the Z coordinate. As the Fourier series can fit any continuous function within the given region, it is easy to approximate the curve by using the Fourier series. In other words, the finite piece method is about to construct an approximation function of the velocity and the extrastress by using the finite element interpolating polynomial in some directions and by continuous smooth Fourier series fitting the boundary conditions in other directions. Assuming that:

$$\mathbf{S} = \sum_{k=1}^{R} \mathbf{S}^k(x,y)F_k(z) = \sum_{k=1}^{R}\sum_{i=1}^{M} w_i(x,y)S_i^k F_k(z) = \sum_{k=1}^{R}\sum_{i=1}^{M} W_i^k S_i^k \tag{25}$$

$$\mathbf{V} = \sum_{k=1}^{R} \mathbf{V}^k(x,y)F_k(z) = \sum_{k=1}^{R}\sum_{i=1}^{M} \phi_i(x,y)\mathbf{V}_i^k F_k(z) = \sum_{k=1}^{R}\sum_{i=1}^{M} \Phi_i^k \mathbf{V}_i^k \quad (26)$$

The pressure approximation function still is:

$$p = \sum_{i=1}^{N} \varphi_i(x,y)p_i \quad (27)$$

In the equations, the velocity $\mathbf{V}$ include the components v_x and v_y; the extrastress $\mathbf{S}$ include the components S_{xx},S_{yy},S_{xy},S_{xz},S_{yz}; $F_k(z)$ is Fourier series which meet the boundary conditions in the thickness direction; S_i^k, V_i^k are the nodal extrastress and velocity corresponding to the kth item of the series, respectively; p_i is the node pressure; w_i (x,y), ϕ_i (x,y), φ_i (x,y) are respectively, the shape function of extrastress, velocity, and pressure; $W_i^k = w_i(x,y)F_k(z)$, $\Phi_i^k = \phi_i(x,y)F_k(z)$; M is total number of the node with stress and velocity; N is total number of the node with pressure, R is the total number of the term taken in the series.

In this article, we use quadrilateral elements with a quadratic interpolation for the velocity and extrastress, a linear interpolation for the pressure field. According to above ideas, the element can only be divided in the X-Y plane, but the "element" is the pieces $11'22'33'44'$ with certain thickness of channels, as shown in Figure 2, thus it is called the finite piece method. For the finite elements method, the elements are connected by nodes but for the finite piece method they are connected by lines, for example $22'$, $33'$, and $44'$ in Figure 2. After the approximation function of X-Y plane is constructed, according to eqs. (25) and (26), the velocity and extrastress distributions of the entire region can be determined.

For a viscoelastic fluid (PTT constitutive equation), to overcome the effects of convection term the inconsistent SU method[24] is adopted here and an additional term of the weighted function is introduced:

$$\bar{W}_i^k = \frac{\bar{k}\mathbf{V}}{(\mathbf{V}\cdot\mathbf{V})}\cdot\nabla W_i^k \quad (28)$$

the coefficient $\bar{k}$ is defined by the velocity components v_ξ and v_η at the element center:

$$\bar{k} = (v_\xi^2 + v_\eta^2)^{1/2}\Big/2 \quad (29)$$

The Galerkin weighted residual method is adopted for the discretization of eqs. (1), (7), and

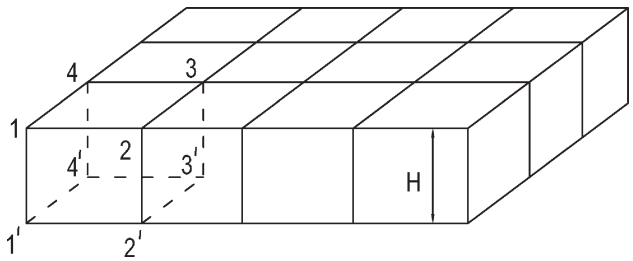

Figure 2 The finite piece mesh with thickness H.

(24) where let residual value equal to W_i^k, Φ_i^k, and φ_i. The additional term only affects the purely advective term of the constitutive equations and the following elemental equations are obtained:

$$\int_\Omega (W_i^k(Y(S)\mathbf{S} + \lambda((1-\xi/2)\overset{\nabla}{\mathbf{S}} + (\xi/2)\overset{\Delta}{\mathbf{S}}) - 2\eta_v\mathbf{D})d\Omega + \int_\Gamma \bar{W}_i^k\lambda\mathbf{V}\cdot\nabla\mathbf{S}d\Omega = 0 \quad (30)$$

$$\int_\Omega (\nabla\Phi_i^k)^{\mathrm{T}}\cdot(-p\mathbf{I}+\tau)d\Omega = \int_\Gamma \mathbf{t}\Phi_i^k d\Gamma \quad (31)$$

$$\int_\Omega \varphi_i\nabla\cdot\mathbf{q}d\Omega = 0 \quad (32)$$

In the equations, $\boldsymbol{t}$ is the known surface force, q is the volumetric flow.

The Picard iteration method is applied to solution of above nonlinear equations. The algorithm of the numerical method is described by a flow chart in Figure 3. Indeed, let $\mathbf{S}^{(n)}$, $\mathbf{V}^{(n)}$, $\mathbf{q}^{(n)}$, and $p^{(n)}$ denote respectively, the values of polymeric stress tensor, velocity, volumetric flow and pressure after last iteration, we use below relation:

$$\tau^{(n+1)} = \mathbf{S}^{(n)} + \eta_s(\nabla\mathbf{V}^{(n+1)} + \nabla\mathbf{V}^{(n+1)\mathrm{T}}) \quad (33)$$

Substituting it into eqs. (31) and (32):

$$\int_\Omega \left(-P^{(n+1)} + 2\eta\frac{\partial v_x^{(n+1))}}{\partial x}\right)\frac{\partial\Phi_i^k}{\partial x}d\Omega + \int_\Omega \eta\left(\frac{\partial v_x^{(n+1)}}{\partial y} + \frac{\partial v_y^{(n+1)}}{\partial x}\right)\frac{\partial\Phi_i^k}{\partial y}d\Omega + \int_\Omega \eta\frac{\partial\delta v_x^{(n+1)}}{\partial z}\frac{\partial\Phi_i^k}{\partial z}d\Omega = -\int_\Omega \left(-P + \frac{\partial S_{xx}^{(n)}}{\partial x}\right)\frac{\partial\Phi_i^k}{\partial x}d\Omega - \int_\Omega \frac{\partial S_{yx}^{(n)}}{\partial y}\frac{\partial\Phi_i^k}{\partial y}d\Omega - \int_\Omega \frac{\partial S_{zx}^{(n)}}{\partial z}\frac{\partial\Phi_i^k}{\partial z}d\Omega + \int_\Gamma t_x\Phi_i^k d\Gamma \quad (34)$$

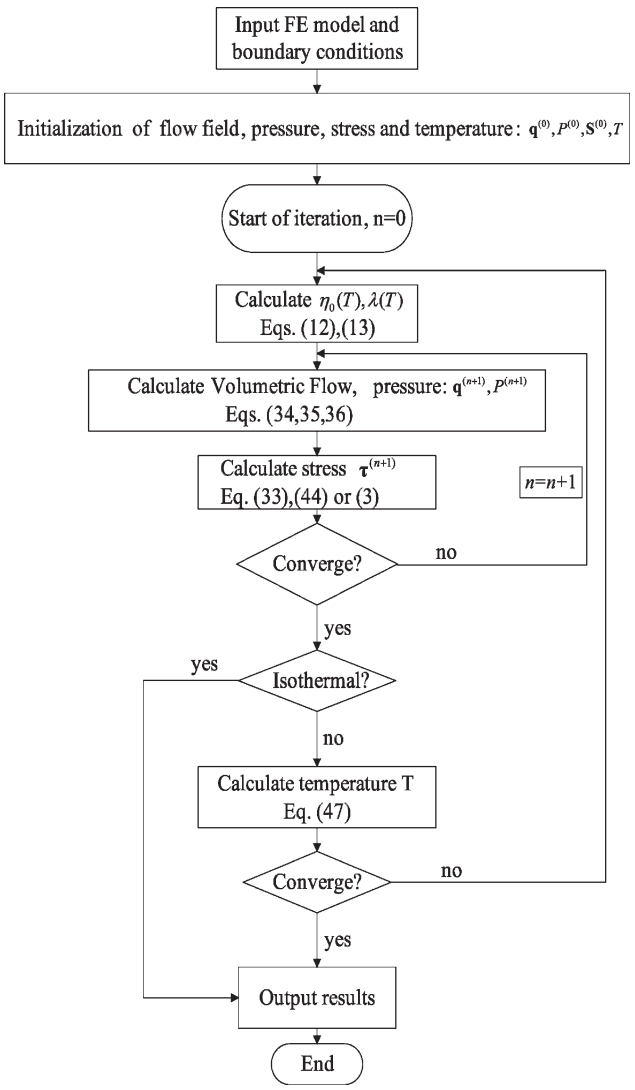

Figure 3 Flow chart of the computational procedure.

$$\int_\Omega \eta\left(\frac{\partial v_y^{(n+1)}}{\partial x}+\frac{\partial v_x^{(n+1)}}{\partial y}\right)\frac{\partial \Phi_i^k}{\partial x}d\Omega$$
$$+\int_\Omega\left(-P^{(n+1)}+2\eta\frac{\partial v_y^{(n+1)}}{\partial y}\right)\frac{\partial \Phi_i^k}{\partial y}d\Omega+\int_\Omega \eta\frac{\partial v_y^{(n+1)}}{\partial z}\frac{\partial \Phi_i^k}{\partial z}d\Omega$$
$$=-\int_\Omega\frac{\partial S_{xy}^{(n)}}{\partial x}\frac{\partial \Phi_i^k}{\partial x}d\Omega-\int_\Omega\left(-P+\frac{\partial S_{yy}^{(n)}}{\partial y}\right)\frac{\partial \Phi_i^k}{\partial y}d\Omega$$
$$-\int_\Omega\frac{\partial S_{zy}^{(n)}}{\partial z}\frac{\partial \Phi_i^k}{\partial z}d\Omega+\int_\Gamma t_y\Phi_i^k d\Gamma \quad (35)$$

$$\int_\Omega\left(\frac{\partial q_x^{(n+1)}}{\partial x}+\frac{\partial q_y^{(n+1)}}{\partial y}\right)\phi_i d\Omega=0 \quad (36)$$

Moreover, eqs. (34) and (35) are tenable only when they are used inside the element. The velocity values of the same nodes in different elements with different thickness are not equal; however, the volumetric flow values are equal. Thus eqs. (34) and (35) are converted into equations with volumetric flow as the unknown variables to combine the element equations into a global equation.

In this article, we only use the first item of series, so the velocity is given by following form:

$$v_x(x,y,z)=v_x(x,y)\sin\left(\frac{\pi}{H}z\right) \quad (37)$$
$$v_y(x,y,z)=v_y(x,y)\sin\left(\frac{\pi}{H}z\right) \quad (38)$$

H is the thickness of the channel, integrating along the thickness, one obtains:

$$q_x(x,y)=\int_0^H v_x(x,y,z)dz=\frac{2H}{\pi}v_x(x,y) \quad (39)$$
$$q_y(x,y)=\int_0^H v_y(x,y,z)dz=\frac{2H}{\pi}v_y(x,y) \quad (40)$$

Substitute for v_x, v_y in eqs. (34) and (35) and change Φ_i^k to $\Phi_i=\phi_i\sin\left(\frac{\pi}{H}z\right)$, we can obtain following FEM equations with the variable of volumetric flow.

$$A_{ij}q_{xj}+C_{ij}q_{yj}-D_{in}P_n=X_i \quad (41)$$
$$C_{ji}q_{xj}+B_{ij}q_{yj}-E_{in}P_n=Y_i \quad (42)$$
$$D_{jn}q_{xj}+E_{jn}q_{yj}=0 \quad (43)$$

X_i and Y_i are the right-side items of eqs. (34), (35) i and j indicate the number of the velocity node, n is the number of the pressure node, and:

$$A_{ij}=\frac{\pi}{2H}\left(\int_\Omega 2\eta\frac{\partial\Phi_j}{\partial x}\frac{\partial\Phi_i}{\partial x}d\Omega+\int_\Omega\eta\frac{\partial\Phi_j}{\partial y}\frac{\partial\Phi_i}{\partial y}d\Omega+\int_\Omega\eta\frac{\partial\Phi_j}{\partial z}\frac{\partial\Phi_i}{\partial z}d\Omega\right)$$
$$B_{ij}=\frac{\pi}{2H}\left(\int_\Omega\eta\frac{\partial\Phi_j}{\partial x}\frac{\partial\Phi_i}{\partial x}d\Omega+\int_\Omega 2\eta\frac{\partial\Phi_j}{\partial y}\frac{\partial\Phi_i}{\partial y}d\Omega+\int_\Omega\eta\frac{\partial\Phi_j}{\partial z}\frac{\partial\Phi_i}{\partial z}d\Omega\right)$$
$$C_{ij}^{kl}=\frac{\pi}{2H}\int_\Omega\eta\frac{\partial\Phi_j}{\partial x}\frac{\partial\Phi_i}{\partial y}d\Omega,$$
$$D_{in}=\int_\Omega\varphi_n\frac{\partial\Phi_i}{\partial x}d\Omega,\quad E_{in}=\int_\Omega\varphi_n\frac{\partial\Phi_i}{\partial y}d\Omega.$$

The unknown variable of eqs. (41), (42), and (43) is the volumetric flow q. Because the volumetric

TABLE I
Material Parameters of LLDPE for PTT Model

Parameter	η_v (Pa s)	η_s (Pa s)	λ	ξ	ε
Value	11830	1479	0.46	0.01	0.1

flow is continuous at nodes, the global stiffness matrix equation for all the elements can be assembled after the elemental calculation.

By the finite piece method, we divide element with thickness only in the XY plane. Compared with 3D FEM, the number of the elements becomes much less, and the preprocessing becomes more simple.

The extrastress tensor $\mathbf{S}$ in X_i and Y_i of eqs. (41) and (42) is calculated by solving linear eq. (30). The iterative algorithm is given by following form:

$$\int_\Omega (W_i^k(Y(\mathbf{S}^{(n)})\mathbf{S} + \lambda((1-\xi/2)\overset{\nabla}{\mathbf{S}}^{(n+1)} + (\xi/2)\overset{\Delta}{\mathbf{S}}^{(n+1)}) - 2\eta_v\mathbf{D}^{(n)})d\Omega + \int_\Gamma \bar{W}_i^k\lambda\mathbf{V}^{(n)}\cdot\nabla\mathbf{S}^{(n+1)}d\Omega = 0 \quad (44)$$

In the equations, $\mathbf{S}^{(n)}$, $\mathbf{V}^{(n)}$, and $\mathbf{D}^{(n)}$ denote respectively, the values of polymeric stress tensor, velocity, and rate of strain tensor after last iteration. The extrastress tensor is assumed to be following form according to the boundary conditions:

$$S_{ij}(x,y,z) = S_{ij}(x,y)\sin\left(\frac{\pi}{H}z\right), \quad i,j = x,y \quad (45)$$

$$S_{ij}(x,y,z) = S_{ij}(x,y)\cos\left(\frac{\pi}{H}z\right), \quad i = x,y; j = z \quad (46)$$

If the flow is nonisothermal, after the flow and stress fields are solved, a second iteration loop is necessary to calculate the temperature field by using a finite-difference method given by Arpin.[11] The temperature field is considered 3D and the thermal balance

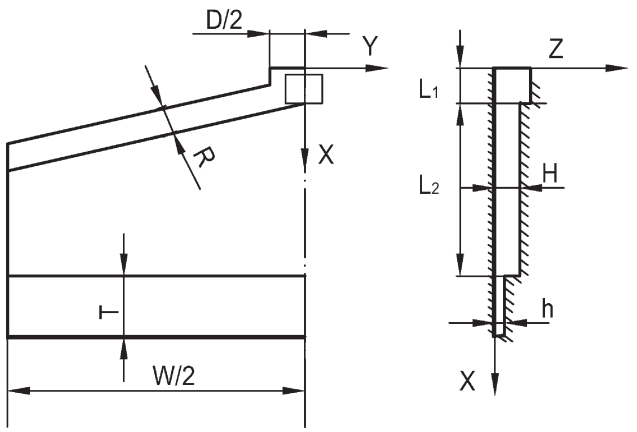

Figure 4 Schematic diagram of the coat-hanger die channel and the coordinate system.

TABLE II
Geometric Parameters of the Fishtail Die (mm)

W_1	W_2	L_1	L_2	T	H_1	H_2
65	500	80	253	50	4	2

includes convection in the X and Y direction, viscous dissipation and conduction through the walls. Conduction in X and Y can be neglected. For the steady flow, the energy eq. (11) can be written as:

$$\rho C_p\left(v_x\frac{\partial T}{\partial x} + v_y\frac{\partial T}{\partial y}\right) = k\frac{\partial^2 T}{\partial z^2} + \tau : \mathbf{D} \quad (47)$$

The global algorithm is illustrated in Figure 3.

SIMULATIONS OF MELT FLOWS IN SHEET DIES

Isothermal results

Because the simulations of fluids obeying PTT constitutive equations are usually used to investigate the accuracy and efficiency of the numerical technique, the isothermal flows of LLDPE in both the fishtail and coat-hanger dies are analyzed respectively, using PTT model and the results are compared with the 3D FEM.

The Material parameters of LLDPE are given in Table I.[25] Boundary conditions are imposed according to the extrudate flow characteristics in the channel. Average velocity for the required flow rate is imposed at the entry section. The volumetric flow rate $Q = 1\ \mathrm{cm}^3/s$. As for fully developed flow at the exit section, velocity components perpendicular to the die axis X and the traction force along the axis X are specified to be zero. Nonslip condition is imposed on the stationary solid wall. The symmetry condition is imposed on the X-Z symmetry plane.

The major features of the flow for the fishtail die have been given in Figure 1. A typical coat-hanger die consists of a manifold and a slit section as shown in Figure 4. The geometric parameters used for the simulation are given in Table II and III. To simplify the mesh of the coat-hanger die, the section of manifold is treated as square. The simulating of the 3D finite element is carried out using the method given by Crochet.[26] The finite element meshes for the 3D approach are displayed in Figure 5 and 6. Because of symmetry the flow in a quarter of the channel is analyzed. The flow region is divided into

TABLE III
Geometric Parameters of the Coat-Hanger Die (mm)

D	W	L_1	L_2	T	R	H	h
10	204	10	82	26	3.1	2.5	1

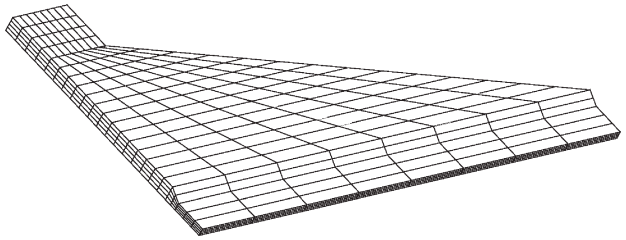

Figure 5 The 3D finite elements mesh of the fishtail die.

3D elements by using mapping mesh generation technology. The number of element divisions along thickness is 4. To compare the results, the mesh of the finite piece method is the same as that of the 3D FEM in *X*-*Y* plane.

Comparisons of simulation results by the finite piece method to the 3D FEM are shown. Figure 7 and 8 show the volumetric flow distributions q_x/q_0 in the lateral scan on the exit. Where q_x is the flow rate of unit width which is calculated according to eq. (21), q_0 is the average flow rate at the entry. By comparison, we find that the results of the finite piece method are in good agreement with the predictions of the 3D FEM. The discrepancy at all points is less than 1.2%. Moreover, it can be seen that the velocity profile of the coat-hanger die gets flatter than the fishtail die. Figure 9 and 10 show the volumetric flow distributions on the *X*-*Z* symmetry plane ($y = 0$). The predictions based on the finite piece method are quite close to those based on the complete 3D simulation except at the contraction mouth. And the discrepancies are restricted to a small region. The discrepancies can be easily understood because the flow channel with varying thickness was divided into parallel regions for the finite piece method.

Figure 11 and 12 show the contours of pressure given by the finite piece method. The pressure distributions on the *X*-*Z* symmetry plane based on the two numerical approaches are plotted in Figure 13 and 14. The results of 3D FEM are the average pressure along the thickness. By analyzing the results of 3D FEM, we found the discrepancies of pressure

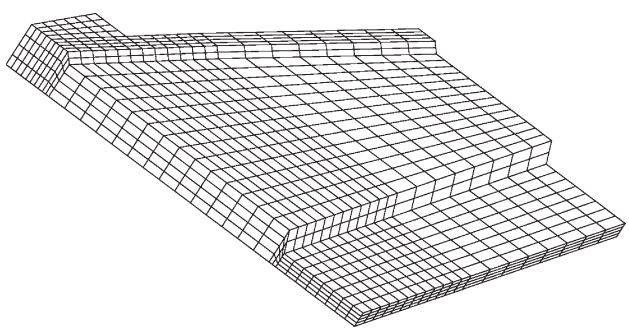

Figure 6 The 3D finite elements mesh of the coat-hanger die.

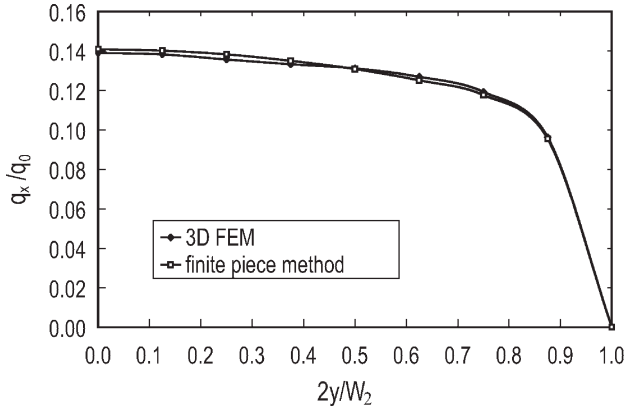

Figure 7 Axial flow rate profile predicted by the finite piece method and the 3D FEM in the exit section of the fishtail die.

along the thickness direction are less than 2%. It can be concluded that it is reasonable to assume that the pressure does not change along the thickness. We observe that there is an abrupt variation in the trend of pressure distribution near the contraction mouth. Because of thinner channel, the pressure drop of coat-hanger dies is greater than the fishtail die. Overall, for two kinds of dies the pressure obtained by the finite piece method shows satisfactory agreement with the results of 3D FEM. It can be seen the pressure predicted by the finite piece method is slight smaller than 3D FEM but not exceeding 6%. And the large discrepancies are restricted to a small region. This can be explained by the fact that the surface force components of wall in *X*,*Y* direction are ignored, and only the first item of Fourier series is utilized to approach the velocity distributions along the *Z* direction. However, the pressure drop caused by the shear viscosity in the slit region is more significant than the normal stresses of the converging section, and the surface force of *X*, *Y* direction has little influence on the results of the pressure

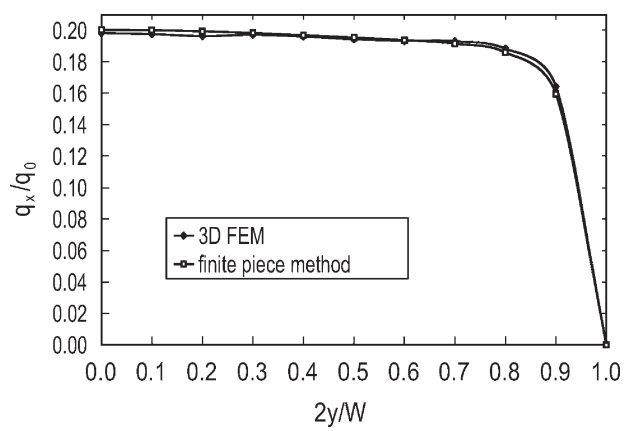

Figure 8 Axial flow rate profile predicted by the finite piece method and the 3D FEM in the exit section of the coat-hanger die.

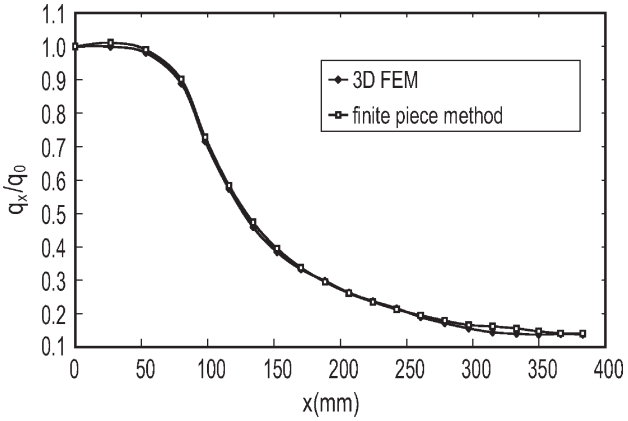

Figure 9 Axial flow rate profile predicted by the finite piece method and the 3D FEM in the *X-Z* symmetrical plane of the fishtail die.

for sheet dies. Accordingly there is a minor discrepancy between the results obtained from the finite piece method and the 3D FEM.

The most significant contribution of the finite piece method is that a substantial amount of CPU time and memory requirement can be saved. In this article convergent criterion is set to 10^{-4} and the computational data are shown in Table IV. It can be seen that the number of the unknowns in the finite piece method is far less than that of 3D FEM. This is because the number of its elements is quarter for the 3D mesh and the unknowns of nodal velocity are reduced from three to two ($v_z = 0$). Accordingly, the memory requirement is significantly reduced, and CPU time per iteration can be saved by more than 80%. We also found the number of iterations is very close to that of the 3D FEM. This shows that it does not decrease the rate of convergence to predict velocity distributions by Fourier series.

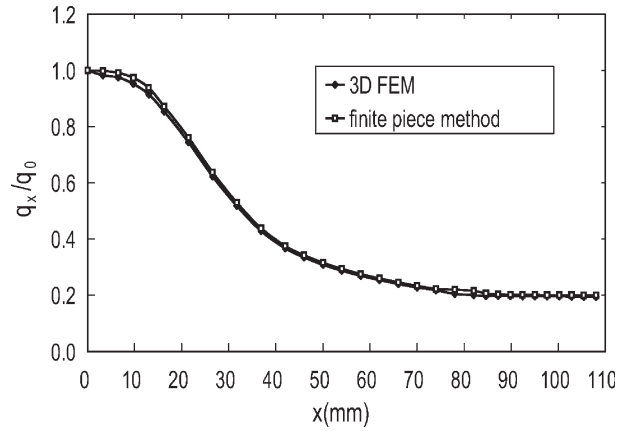

Figure 10 Axial flow rate profile predicted by the finite piece method and the 3D FEM in the *X-Z* plane symmetrical of the coat-hanger die.

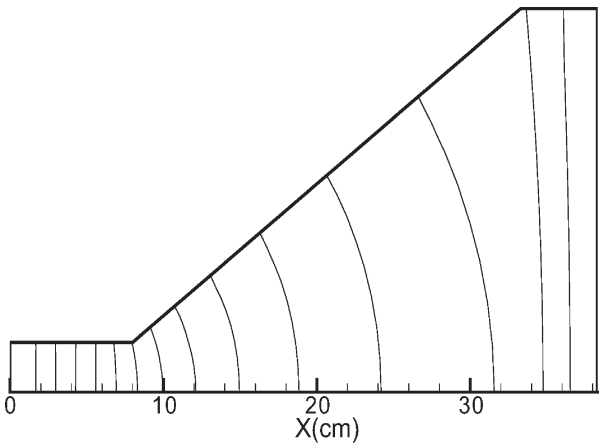

Figure 11 The contours of pressure in the fishtail die predicted by the finite piece method.

Nonisothermal results

The simulations of LLDPE nonisothermal flows in the coat-hanger die were carried out using Carreau-Yasuda model also. The uniformity index[27] and the pressure drop are compared with the results from Arpin's experiment. The rheological coefficients of LLDPE have been given in Ref. 11. The temperature field is calculated by using a finite-difference method. The boundary conditions are applied in accordance with experiment. The die wall is assumed to be adiabatic: $\frac{\partial T}{\partial z} = 0$.

The uniformity index was created to analyze the performance of flat dies which has been used up to now. Computing the uniformity index is a good qualitative comparison tool. Separating the die into

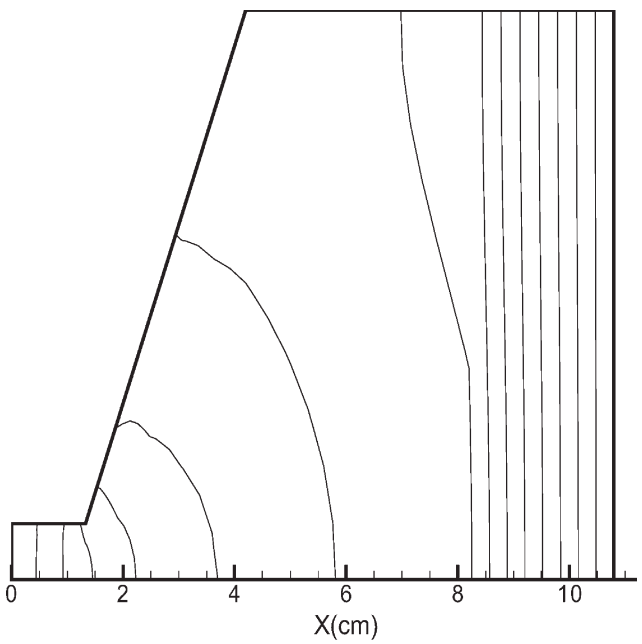

Figure 12 The contours of pressure in the coat-hanger die predicted by the finite piece method.

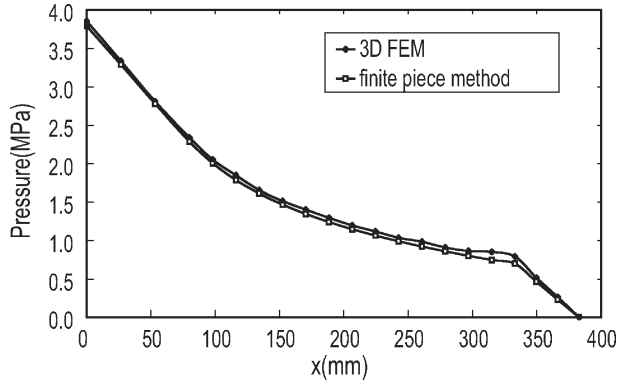

Figure 13 Pressure predicted by the finite piece method and the 3D FEM in the *X-Z* symmetrical plane of the fish-tail die.

N sections across the width, the uniformity index is defined as:

$$U = 1 - \left| \frac{1}{N} \sum_{i=1}^{N} \left(N \frac{Q_i}{Q} - 1 \right)^2 \right|^{1/2} \tag{48}$$

where Q_i is volumetric flow through i-th section, Q is total volumetric flow.

To investigate the sensitivity of the simulation results with respect to the mesh size, we computed the numerical solution on three meshes. The mesh data in Table V comprise the total number of element and node, degrees of freedom (DOF) and the minimum mesh spacing normalized with the width W ($R_{\min}$).

Figure 15 shows the numerical prediction for the uniformity index as a function of the volumetric flow rate in comparison with the experimental data. The overall agreement of the uniformity index between the finite piece method and the experiment is good except for the individual point. The maximum error is about 2.3%.

The overall pressure drop versus volumetric flow rate is shown in Figure 16. It can be seen that the predicted pressure levels off at the highest flow rates after an initial rapid increase, similar to the experimental data. However, the pressure drop prediction is smaller than experimental. With the increasing of the flow rate, the discrepancy becomes larger, and ultimately reaches 5.6% (M1).

We can observe in Figure 15 and 16 that the numerical solutions obtained using the three meshes are in good agreement. Using a mesh size ($R_{\min}$) of 0.0056 instead of 0.00167, which is one-third the size, gives a uniformity index that is only 0.5% lower, and the pressure drop increases by 2.8%. Moreover, we can see that as the mesh is refined the numerical solutions converge to the experimental data. The

TABLE IV
Comparison of Computational Data Between the Finite Piece Method and the 3D FEM

	Fishtail die		Coat-hanger die	
Method	3D FEM	finite piece method	3D FEM	finite piece method
Degrees of node	10	8	10	8
No. of node	3939	615	12621	1981
No. of element	736	184	2496	624
No. of unknowns	36531	4521	116984	14546
No. of iteration	22	23	25	27
CPU time(s)	946	207	3650	486
CPU time(s)/iteration	43	9	146	18

TABLE V
Major Characteristics of the Computational Meshes

Mesh	M1	M2	M3
elements	624	1448	2472
nodes	1981	4503	7625
DOF(V, p)	4641	10534	17827
$R_{\min}$	0.0167	0.0084	0.0056

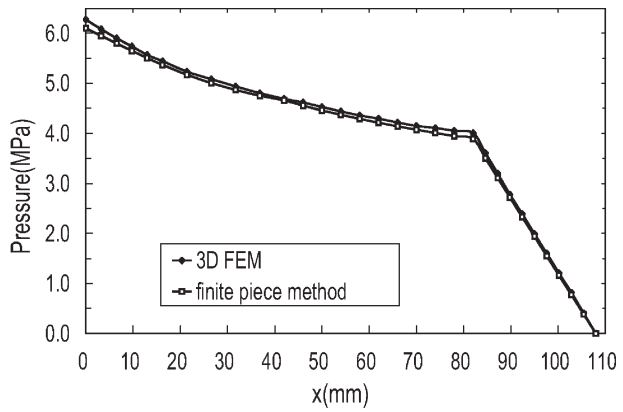

Figure 14 Pressure predicted by the finite piece method and the 3D FEM in the *X-Z* symmetrical plane of the coat-hanger die.

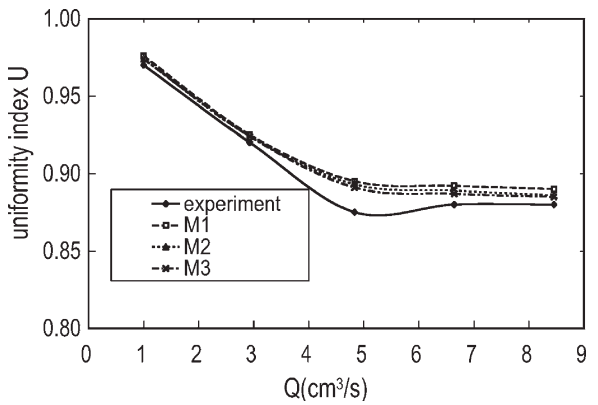

Figure 15 Prediction of the uniformity index for the coat-hanger die as a function of the flow rate in comparison with experimental data.

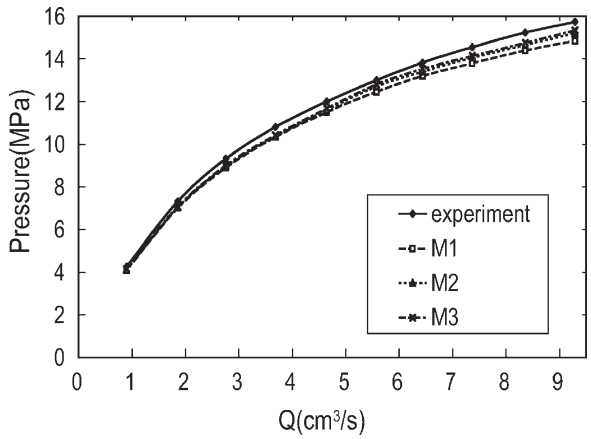

Figure 16 Prediction of the pressure drop for the coat-hanger die as a function of the flow rate in comparison with experimental data.

coarse mesh M1 leads to a larger uniformity index and a smaller pressure drop. For this die, considering the sufficient accuracy and computationally cost-effective, mesh M2 is a good comprise which corresponds to 40 elements across the half-width.

CONCLUSIONS

In this study, a new finite element technique named the finite piece method is proposed to simulate the viscoelastic polymer flow in the sheet dies. In this method, the distributions of velocities are approached using the approximating polynomial in the *X*-*Y* plane and Fourier series in *Z* direction. The mesh is divided in *X*-*Y* plane, so the 3D flow problem is reduced to the 2D case.

Analyzing the behavior of the polymer melt flow through the fishtail and coat-hanger dies has been carried out by both the finite piece method and the 3D FEM. The results of the finite piece element are compared with those of the 3D FEM simulations and Arpin's experiments. The solution accuracy is excellent for most of the cases presented although some assumptions were made to simplify the problem. The volumetric flow distributions obtained by the finite piece method show satisfactory agreement with that of 3D FEM. At the die exit the relative error between the two methods is below 1.2%. There is a minor discrepancy between the pressure distributions obtained by the finite piece method and the 3D FEM. For the whole die, the discrepancies caused by varying thickness of channel are restricted to a small region, and it does not exceed 6%. For the finite piece method, the memory requirement is significantly reduced, and CPU time per iteration can be saved by more than 80%. The overall agreement of the uniformity index between the finite piece method and Arpin's experiment is satisfactory except for the individual point in which the error is about 2.3%. The pressure drop prediction of the finite piece method on the whole is not as close to the experiment as to the volumetric flow distributions. The maximum discrepancy reaches 5.6% (M1). It may be attributed to the following reasons: (1) the material parameters in the constitutive equation are not accurate enough. (2) Only the first item of Fourier series is utilized to approach the velocity distributions along the *Z* direction at high shear rates. (3) Nonslip condition is imposed on the solid wall.

It is concluded that the finite piece method is effective in simulating the slit flow in the sheet dies. Owing to little demand on computational memory, the finite piece method can be used to solve large-scale 3D problems.

It can be inferred that the space slit flow can be analyzed by the finite piece method too. One of further work is to give the way to solve space problem by this method. Furthermore, the finite piece method combined with the 3D FEM to simulate the flow in the complex 3D channel is another future issue.

References

1. Xinhou, W.; Ting, C.; Xiubao, H. J Appl Polym Sci 2006, 101, 1570.
2. Kai, M.; Xinhou, W.; Xiubao, H. J Appl Polym Sci 2008, 108, 2523.
3. Gifford, W. A. Polym Eng Sci 2000, 40, 2095.
4. Gifford, W. A. Polym Eng Sci 2001, 41, 1886.
5. Nadhir, L.; Fabrice, S.; Stephan, P.; Daniel, S. Polym Eng Sci 2009, 49, 432.
6. Hieber, C. A.; Shen, S. F. J Non-Newton Fluid Mech 1980, 7, 1.
7. Vlcek, J.; Mailvaganam, G. N.; Vlachopoulos, J.; Perdikoulias, J. Adv Polym Tech 1990, 10, 309.
8. Liu, L.; Wen, S.; Liu, T. Adv Polym Tech 1994, 13, 283.
9. Yunwey, Y.; Tajo, L. Polym Eng Sci 1999, 39, 144.
10. Tingqi, W.; Bo, J.; Shuhua, X.; Nabin, H. J Appl Polym Sci 2006, 101, 2911.
11. Arpin, B.; Lafleur, P. G.; Sanschagrin, B. Polym Eng Sci 1994, 34, 657.
12. Ifford, W. A. Polym Eng Sci 1998, 38, 1729.
13. Qi, W.; Douglas, E. S. J Appl Polym Sci 2007, 103, 3994.
14. Douglas, E. S.; Qi, W. Polym Eng Sci 2005, 45, 953.
15. Douglas, E. S. Int J Numer Meth Eng 2003, 57, 1381.
16. Phan, T. N. J Rheol 1978, 22, 259.
17. Alves, M. A.; Oliveira, P. J.; Pinho, F. T. J Non-Newtonian Fluid Mech 2003, 110, 45.
18. Alves, M. A.; Pinho, F. T.; Oliveira, P. J. J Rheol 2003, 52, 1347.
19. Yue, M.; Guoqun, Z.; Chengrui, Z.; Anbiao, C.; Huiping, L. Int J Numer Meth Fluids 2010, 63, 811.
20. Manuel, A. A.; Paulo, J. O.; Fernando, T. P. J Non-Newtonian Fluid Mech 2003, 110, 45.
21. Aboubacar, M.; Matallah, H.; Webster, M. F. J Non-Newtonian Fluid Mech 2002, 103, 65.
22. Yue, M.; Guoqun, Z.; Chengrui, Z. J Appl Polym Sci 2010, 117, 91.
23. Tome, M. F.; Pauloa, G. S.; Pinho, F. T.; Alves, M. A. J Non--Newtonian Fluid Mech 2010, 165, 247.
24. Marchal, J. M.; Crochet, M. J. J Non-Newtonian 1987, 6, 77.
25. William, H. H.; Donald, G. B. J Non-Newtonian Fluid Mech 1996, 65, 247.
26. Crochet, M. J.; Davies, A. R.; Walters, K. Numerical of Non-Newtonian Flow; Elsevier Science Publishers: Amsterdam, 1984, Chapter 8.
27. Mckelvey, J. M.; Ito, K. Polym Eng Sci 1971, 11, 258.